nature photonics

LETTERS

https://doi.org/10.1038/s41566-019-0452-0

Photonic quadrupole topological phases

Sunil Mittal[1,2*], Venkata Vikram Orre[1,2], Guanyu Zhu[1,2], Maxim A. Gorlach[3], Alexander Poddubny[3,4,5] and Mohammad Hafezi[1,2,6]

The topological phases of matter are characterized using the Berry phase, a geometrical phase associated with the energy-momentum band structure. The quantization of the Berry phase and the associated wavefunction polarization manifest as remarkably robust physical observables, such as quantized Hall conductivity and disorder-insensitive photonic transport[1–5]. Recently, a novel class of topological phases, called higher-order topological phases, were proposed by generalizing the fundamental relationship between the Berry phase and quantized polarization, from dipole to multipole moments[6–8]. Here, we demonstrate photonic realization of the quantized quadrupole topological phase, using silicon photonics. In our two-dimensional second-order topological phase, we show that the quantization of the bulk quadrupole moment manifests as topologically robust zero-dimensional corner states. We contrast these topological states against topologically trivial corner states in a system without bulk quadrupole moment, where we observe no robustness. Our photonic platform could enable the development of robust on-chip classical and quantum optical devices with higher-order topological protection.

The Berry phase provides a universal framework that relates the robust quantization of physical observables at the boundaries of a non-interacting system to the topological properties of the bulk. For example, in electronic systems, the Berry phase dictates the presence of quantized zero-dimensional (0D) charges in 1D insulators[1,2], quantized charge/spin currents along the 1D edges of 2D quantum Hall/spin Hall systems[3,9], and conducting 2D surfaces in 3D topological insulators[10]. In general, this bulk–boundary correspondence relates the quantized charge/current carried by the $(n-1)$-dimensional boundaries to the quantized electric dipole moment of the n-dimensional bulk[4]. Recently, this relationship between the charge moments of the bulk and their boundary manifestations has been generalized from electric dipole to multipole moments, leading to higher-order topological phases[6–8,11]. For example, a quantized quadrupole moment in a 2D system leads to the presence of quantized charges, which are localized at the 0D corners. This is in contrast to the quantized dipole moment, which gives rise to 1D edge currents in a 2D system.

When formulated in terms of the Berry phase, the bulk–boundary correspondence also applies to neutral bosonic systems; that is, the non-trivial topology of the bulk leads to the emergence of robust boundary states. In fact, topologically robust, localized 0D edge states in 1D systems and propagating 1D edge states in 2D systems have been realized using atomic[12], photonic[5,13–17] as well as phononic lattices[18]. Motivated by the search for higher-order topological phases, the 2D quadrupole topological phases with robust 0D corner states were recently observed using microwave[19,20] and phononic metamaterials[21–23]. We report on the optical realization of the quadrupole topological phase, employing an integrated silicon photonics platform. Using spectroscopic measurements and direct imaging, we reveal the existence of the localized corner states and show that they are robust against certain fabrication disorders that are ubiquitous in nanophotonic systems. Furthermore, by introducing a quadrupole domain boundary in our system, we show that the observed corner states are not artefacts at the physical corners of the lattice. We note that the corner states can also emerge in systems without a quadrupole moment[24,25]. We study corner states associated with zero bulk quadrupole moment and observe that they are not immune to fabrication disorders.

Our quadrupole topological system is realized using a 2D lattice of nanophotonic silicon ring resonators (Fig. 1; see Methods for details of device fabrication). The unit cell (plaquette) of this lattice consists of four site rings arranged into a square (in blue in Fig. 1). These site rings are evanescently coupled to their nearest neighbours using a set of auxiliary rings, which we call link rings (in green and red). The resonance frequencies of the link rings are detuned from those of the site rings by introducing an extra path length. We control the magnitude of the coupling strength between the lattice sites by adjusting the gap between the site-ring and the link-ring waveguides. Furthermore, the link rings allow us to manipulate the sign (phase) of the coupling between the site rings and introduce a synthetic gauge flux threading each square plaquette[15,26]. Specifically, when the link ring coupling two site rings along the x axis is vertically shifted, the photons hopping towards the right travel a slightly longer path compared to those hopping towards the left (Fig. 1). This path length difference results in an effective, direction-dependent, hopping phase ϕ. We choose $\phi=\pi$ such that the shifted link ring (in red) introduces a negative coupling. In a unit cell, we arrange the link rings such that $\phi\neq 0$ for only one coupling term, while keeping the amplitude of coupling equal to γ. This results in a net gauge flux π threading the unit cell (Fig. 1b and Supplementary Section 1). To implement a topological system with quantized quadrupole moment[6], we realize a 2D array of these unit cells, coupled to their nearest neighbours with coupling strength $\pm\kappa$. Throughout the lattice, we change the sign of the inter-cell coupling κ, such that a uniform gauge flux π penetrates any plaquette (made of a 2×2 array of site rings; Figs. 1b,c and 2a). When $\gamma/\kappa<1$—that is, when the inter-cell coupling is stronger than the intra-cell coupling—the lattice hosts degenerate mid-gap states localized at each of the four corners (Fig. 2b,e and Supplementary Section 2). The corner states are characterized by topologically invariant integers and protected against certain disorders. This topological protection is due to the presence of spatial inversion symmetry, and the two mirror symmetries (about the x and y axes) of the lattice which do not commute because of the non-zero gauge flux[6]. In the other case, that is when

[1]Joint Quantum Institute, NIST/University of Maryland, College Park, MD, USA. [2]Department of Electrical and Computer Engineering and IREAP, University of Maryland, College Park, MD, USA. [3]ITMO University, St Petersburg, Russia. [4]Nonlinear Physics Centre, Australian National University, Canberra, Australian Capital Territory, Australia. [5]Ioffe Institute, St Petersburg, Russia. [6]Department of Physics, University of Maryland, College Park, MD, USA. *e-mail: mittals@umd.edu

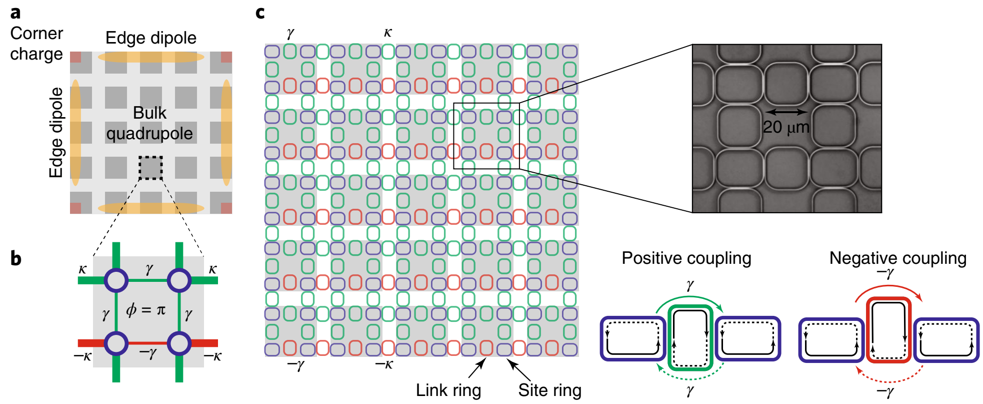

Fig. 1 | Schematic of the photonic quadrupole topological system. **a**, Schematic of the topological system with quantized quadrupole moment in the bulk, which induces quantized dipole moments at the edges and quantized charges at the corners. **b**, The unit cell consists of four lattice sites with nearest-neighbour couplings of magnitude γ. One of the couplings (shown as red) is negative, which introduces a gauge flux $\phi=\pi$ per unit cell. The coupling strength between neighbouring unit cells is $\pm\kappa$. **c**, Schematic of the 2D lattice of ring resonators. The unit cell (each shaded grey) is composed of four site rings (blue), evanescently coupled by four link rings (green and red). The gap between the site and the link-ring waveguides controls the magnitude of inter-/intra-cell couplings. To engineer the negative coupling, the link rings (red) are vertically shifted. The link rings (green) corresponding to positive couplings are not shifted. Inset, microscope image of the plaquette.

$\gamma/\kappa>1$, the lattice is topologically trivial and there are no states in the bandgap (Fig. 2h).

In our experiment, we fabricate a 5×5 array of unit cells, as shown in Fig. 2a. We design the system to be in the topological regime with the coupling strengths γ and κ estimated to be 4.8(2) GHz and 29.0(8) GHz, such that $\gamma/\kappa\approx0.17$. To probe the presence of corner states in the lattice, we fabricate a waveguide coupler at each of the corners (Fig. 2a). This allows us to couple the lattice to a laser and measure the power absorption at each corner as a function of the laser frequency detuning ($\delta\nu$) from the ring resonance frequency (ν). Furthermore, we use a microscope objective and an infrared camera to directly image the spatial intensity profile in the lattice, as we sweep the laser frequency (see Methods for further details). The measured absorption spectra at the four corner sites are shown in Fig. 2d. We observe very narrow absorption peaks, indicating the presence of four isolated mid-gap states in the lattice (Fig. 2b). Figure 2f shows the measured spatial intensity profile in the lattice with each corner excited independently, and integrated over the corresponding absorption peaks. In agreement with numerical simulation (Fig. 2e), we see that the corner modes are remarkably localized at the corner sites. However, contrary to the theoretical prediction (Fig. 2b,c), the absorption peaks are shifted with respect to each other, indicating that the corner states are not degenerate in frequency. This is due to the nanofabrication process, which introduces very strong disorder in the ring resonance frequencies (Supplementary Section 3). The upper bound on the standard deviation in the ring resonance frequencies was measured to be ~33 GHz, which is very significant compared to the bandgap $2\sqrt{2}\kappa\approx68$ GHz. In addition, there is a small disorder in the coupling strengths γ and κ, which was estimated to be ~4% of the mean values, and also a disorder of 0.1 (radians) in the gauge flux ϕ. Remarkably, even in the presence of such strong disorder, which is comparable to the bandgap, the corner states are still present and well localized; this highlights their topological protection. Using numerical simulations, we find that the corner states exist for even stronger disorder in the coupling strengths and also random variations in the sign of coupling (Supplementary Section 4). We note that the 'zero energy' in these measurements corresponds to the resonance frequency of a particular longitudinal mode of the ring resonators.

To show the absence of corner states in a trivial system, we analyse the scenario where the intra-cell hopping is much stronger than the inter-cell hopping, that is, $\gamma/\kappa>1$ (Fig. 2g). For this system we swap the two coupling strengths—that is, now $\gamma\approx29$ GHz and $\kappa\approx4.8$ GHz—such that $\gamma/\kappa\approx5.8$. As such, the lattice is topologically trivial and the mid-gap modes are absent (Fig. 2h). Figure 2j shows the measured power absorption spectra at the four corners and Fig. 2l shows the spatial intensity distribution integrated over the absorption bands. In contrast to Fig. 2d, the spectra in Fig. 2j show two broad absorption bands centred around $\pm\sqrt{2}\gamma$, corresponding to the bulk states of the lattice[6]. Furthermore, the observed spatial intensity distributions (Fig. 2l) confirm that these absorption bands do not correspond to localized modes and are smeared into the bulk of the lattice.

Next, we demonstrate that the observed corner states are not artefacts arising due to some defects at the physical corners of the lattice. We break the periodicity of the inter-cell coupling strength such that it creates a domain boundary, and the unperturbed quadrupole domain now consists of an array of 5×4 unit cells (Fig. 3a). In this configuration, the corners S_2 and S_3 of the quadrupole domain coincide with the physical corners of the lattice, whereas corner sites S_1 and S_4 of the quadrupole domain are shifted from the physical corners, labelled S'_1 and S'_4 in Fig. 3a. As before, the waveguide couplers for absorption measurements are located at the physical corners of the lattice. Figure 3b,c shows the measured absorption spectra. The spectra at corners S_2 and S_3 show a single absorption peak, and the associated spatial intensity distribution (Fig. 3d) shows localized corner states at S_2 and S_3, consistent with our previous observation. However, the spectra measured at corners S'_1 and S'_4 show three absorption peaks. The spatial intensity distribution corresponding to the middle absorption peak around zero frequency detuning, in fact, shows excitation of localized modes at the corners S_1 and S_4 of the quadr'upole domain (Fig. 3d). In contrast, the intensity distribution in the other two sidebands, away from zero detuning, occupies the lattice sites outside the quadrupole domain (Fig. 3e). The power absorption in the middle band is lower relative to the sidebands because the corner states of the quadrupole domain are very weakly coupled to the physical corner.

To further explore the significance of topological protection of the observed corner states in the quadrupole system, we compare them with those emerging in a system with zero quadrupole moment—a 2D extension of the Su–Schrieffer–Heeger model

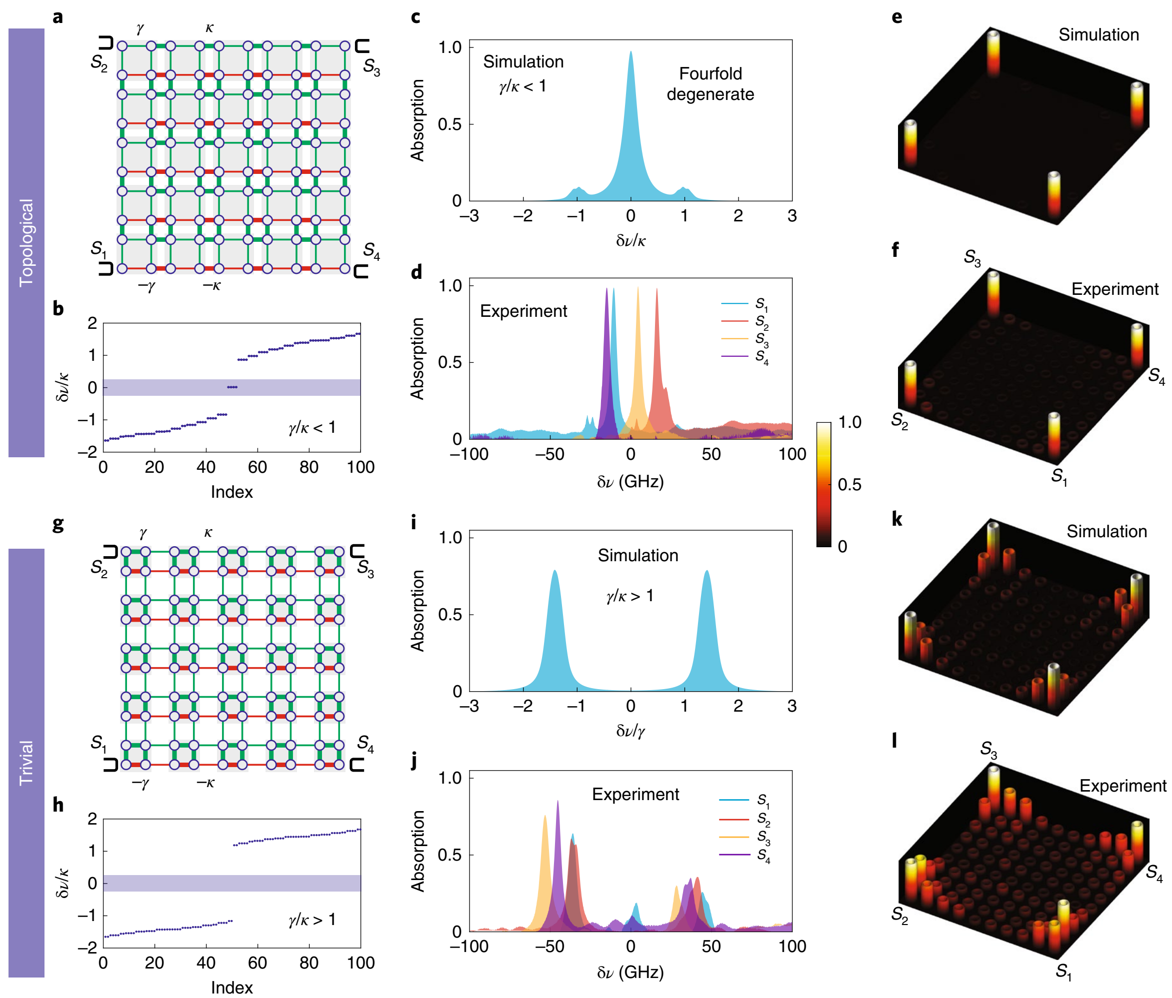

Fig. 2 | Observation of corner states. a, Schematic of the 2D lattice with quantized quadrupole moment. Thick (thin) lines connecting two lattice sites (circles) indicate strong (weak) coupling and their colour indicates positive (green) or negative (red) couplings. The waveguide couplers are located at the four corners. **b**, Energy spectrum for a lattice with a 5×5 array of unit cells, with $\gamma/\kappa < 1$. The four degenerate corner states appear in the bandgap, at zero energy (highlighted in purple). **c**,**d**, Simulated (**c**) and measured (**d**) power absorption spectra at the corners. **e**,**f**, Simulated (**e**) and measured (**f**) spatial intensity profiles (at peak absorption frequencies) in the lattice showing localized corner modes. The intensity profiles are summed over excitations from the four corners. Only the site ring intensities are shown. **g**, Schematic of the trivial 2D lattice with $\gamma/\kappa > 1$. **h**, The bandgap is now devoid of any modes. **i**–**l**, Simulated (**i**,**k**) and measured (**j**,**l**) power absorption spectra (**i**,**j**) and spatial intensity distributions in the absorption bands (**k**,**l**) show an absence of localized modes. The intensity profiles are integrated over the two absorption bands and over the four corners.

(Supplementary Section 6). We fabricated a very similar lattice with zero gauge flux, that is, where all the couplings are positive (Fig. 4a). The inter-cell and intra-cell couplings in this lattice still correspond to the topological case (Fig. 2a), that is, $\gamma/\kappa < 1$. Because of the absence of the gauge flux, the two mirror symmetries (about the x and y axes) commute and the net quadrupole moment is zero (Supplementary Sections 5–7). Numerical simulation, in the absence of disorder, shows that this system hosts zero-energy states localized at the corners, similar to those of the quadrupole system (Fig. 4b,c,e). However, unlike the quadrupole system, the measured absorption spectra at the corners show a multimode structure, indicating that the corner states are not completely isolated from the bulk states (Fig. 4d,f; for additional data see Supplementary Information). The measured spatial intensity distribution confirms that these corner modes indeed couple to the bulk modes of the lattice. This observation suggests that the corner states in the zero gauge flux lattice are susceptible to the fabrication disorder and are not topologically protected. This lack of robustness against disorder is also evident in the energy spectrum of the device, where there is no bandgap at zero energy (Fig. 4b). Consequently, an on-site potential disorder, which is the dominant source of disorder in our experimental set-up, can easily couple these corner states to the bulk states located near zero energy (Supplementary Sections 5 and 6).

Here, we have demonstrated an integrated photonic quadrupole topological system supporting robust corner states immune to disorder in coupling strengths and on-site potential. Our versatile integrated photonics platform opens the route to explore even richer physics in the context of higher-order topological phases, for example, those associated with different choices of gauge flux in the lattice or with asymmetric coupling strengths. Moreover, by integrating active features, for example, using thermal heaters or electro-optic modulators[27], our scheme could allow selective flux insertion or manipulation of the corner/edge modes of the system and hence the realization of adiabatic charge pumping in higher-order topological systems[7]. Furthermore, the integration of gain/loss in this photonics realization could enable the exploration of non-Hermitian physics in the context of higher-order topological phases[28,29]. From a practical perspective, light confinement in the corner states of a

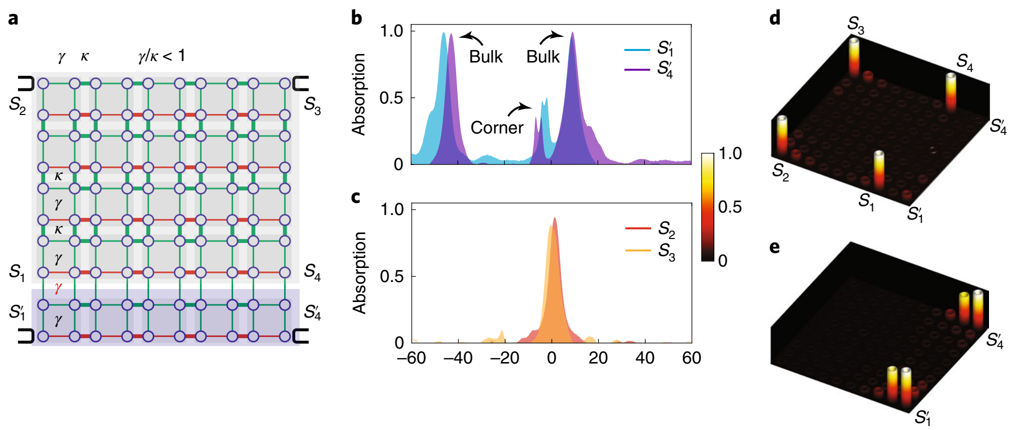

Fig. 3 | Corner states at the quadrupole domain boundary. a, Schematic of the 2D lattice with a quadrupole domain boundary introduced by breaking the periodicity of the inter-cell hopping κ. The bottom corners of the quadrupole are labelled S_1 and S_4 and those of the physical lattice S'_1 and S'_4. Absorption measurements are made at the physical corners of the lattice. **b**,**c**, Measured absorption spectra at the corners. The middle peak in **b**, near zero frequency detuning, corresponds to the corner states of the quadrupole system. **d**, Measured spatial intensity distribution showing localized corner states. The intensity distribution is summed over the single absorption peak for S_2 and S_3 and only over the middle peak for S'_1 and S'_4. **e**, Measured intensity distribution corresponding to the two sidebands, away from zero frequency detuning, of the absorption spectra in **b**. These are bulk modes of the non-quadrupole domain of the lattice.

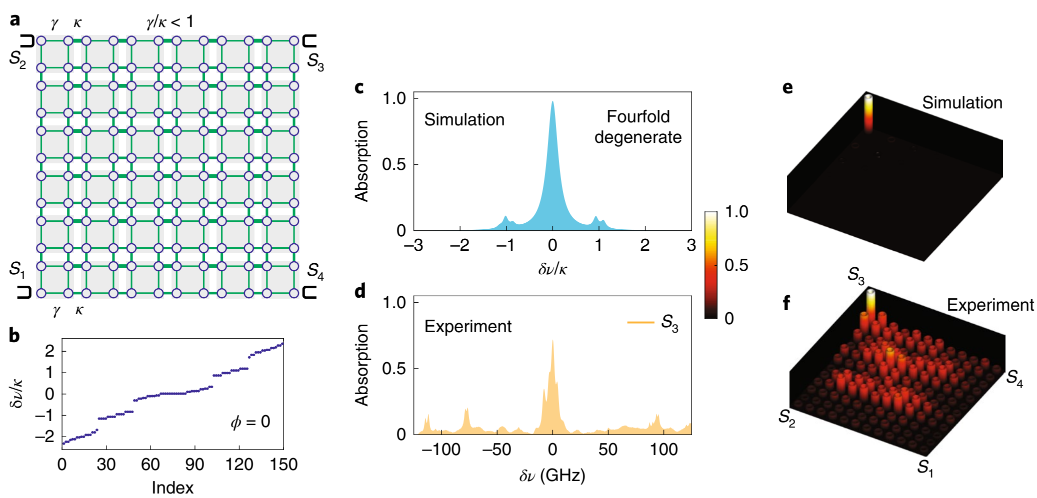

Fig. 4 | Corner states in a lattice with zero gauge flux. a, Schematic of the 2D lattice with $\gamma/\kappa<1$, but all positive couplings (that is, zero gauge flux). We fabricated a 6×6 array of unit cells for this device. **b**, The energy spectrum shows four zero-energy modes with wavefunction localized at the corners, but there is no bandgap at zero energy. **c**, Simulated absorption spectrum at the corner, for a pure system (no disorder), showing predominantly a single absorption peak, similar to that of the quadrupole system. **d**, The corresponding intensity distribution for excitation at corner site S_3 also shows a single mode localized at the corner. **e**,**f**, Experimentally measured absorption at corner S_3 and the corresponding intensity distribution, indicating significant coupling of corner modes to the bulk modes because they are not robust against fabrication disorder (for additional data see Supplementary Information). The intensity distribution is integrated over the absorption band.

topological system inherently realizes robust optical resonators. These could find applications in classical/semiclassical photonic devices such as topological lasers[5], and also in quantum photonics, for example, to implement robust quantum light sources[30], topological quantum amplifiers[31] and enhanced light–matter interactions between topological photonic cavities and quantum emitters[32].

Online content

Any methods, additional references, Nature Research reporting summaries, source data, statements of code and data availability and associated accession codes are available at https://doi.org/10.1038/s41566-019-0452-0.

Received: 21 December 2018; Accepted: 24 April 2019;
Published online: 17 June 2019

References

1. Su, W. P., Schrieffer, J. R. & Heeger, A. J. Solitons in polyacetylene. *Phys. Rev. Lett.* **42**, 1698–1701 (1979).
2. Zak, J. Berry's phase for energy bands in solids. *Phys. Rev. Lett.* **62**, 2747–2750 (1989).
3. Thouless, D. J., Kohmoto, M., Nightingale, M. P. & den Nijs, M. Quantized Hall conductance in a two-dimensional periodic potential. *Phys. Rev. Lett.* **49**, 405–408 (1982).
4. King-Smith, R. D. & Vanderbilt, D. Theory of polarization of crystalline solids. *Phys. Rev. B* **47**, 1651–1654 (1993).
5. Ozawa, T. et al. Topological photonics. *Rev. Mod. Phys.* **91**, 015006 (2019).

6. Benalcazar, W. A., Bernevig, B. A. & Hughes, T. L. Quantized electric multipole insulators. *Science* **357**, 61–66 (2017).
7. Benalcazar, W. A., Bernevig, B. A. & Hughes, T. L. Electric multipole moments, topological multipole moment pumping, and chiral hinge states in crystalline insulators. *Phys. Rev. B* **96**, 245115 (2017).
8. Schindler, F. et al. Higher-order topological insulators. *Sci. Adv.* **4**, eaat0346 (2018).
9. Bernevig, B. A., Hughes, T. L. & Zhang, S.-C. Quantum spin Hall effect and topological phase transition in HgTe quantum wells. *Science* **314**, 1757–1761 (2006).
10. Qi, X.-L. & Zhang, S.-C. Topological insulators and superconductors. *Rev. Mod. Phys.* **83**, 1057–1110 (2011).
11. Schindler, F. et al. Higher-order topology in bismuth. *Nat. Phys.* **14**, 918–924 (2018).
12. Cooper, N. R., Dalibard, J. & Spielman, I. B. Topological bands for ultracold atoms. *Rev. Mod. Phys.* **91**, 015005 (2019).
13. Wang, Z., Chong, Y., Joannopoulos, J. D. & Soljačić, M. Observation of unidirectional backscattering-immune topological electromagnetic states. *Nature* **461**, 772–775 (2009).
14. Kraus, Y. E., Lahini, Y., Ringel, Z., Verbin, M. & Zilberberg, O. Topological states and adiabatic pumping in quasicrystals. *Phys. Rev. Lett.* **109**, 106402 (2012).
15. Hafezi, M., Mittal, S., Fan, J., Migdall, A. & Taylor, J. M. Imaging topological edge states in silicon photonics. *Nat. Photon.* **7**, 1001–1005 (2013).
16. Rechtsman, M. C. et al. Photonic floquet topological insulators. *Nature* **496**, 196–200 (2013).
17. Lu, L., Joannopoulos, J. D. & Soljačić, M. Topological photonics. *Nat. Photon.* **8**, 821–829 (2014).
18. Süsstrunk, R. & Huber, S. D. Observation of phononic helical edge states in a mechanical topological insulator. *Science* **349**, 47–50 (2015).
19. Peterson, C. W., Benalcazar, W. A., Hughes, T. L. & Bahl, G. A quantized microwave quadrupole insulator with topologically protected corner states. *Nature* **555**, 346–350 (2018).
20. Imhof, S. et al. Topolectrical-circuit realization of topological corner modes. *Nat. Phys.* **14**, 925–929 (2018).
21. Serra-Garcia, M. et al. Observation of a phononic quadrupole topological insulator. *Nature* **555**, 342–345 (2018).
22. Xue, H., Yang, Y., Gao, F., Chong, Y. & Zhang, B. Acoustic higher-order topological insulator on a kagome lattice. *Nat. Mater.* **18**, 108–112 (2019).
23. Ni, X., Weiner, M., Alù, A. & Khanikaev, A. B. Observation of higher-order topological acoustic states protected by generalized chiral symmetry. *Nat. Mater.* **18**, 113–120 (2019).
24. Noh, J. et al. Topological protection of photonic mid-gap defect modes. *Nat. Photon.* **12**, 408–415 (2018).
25. Li, F.-F. et al. Topological light-trapping on a dislocation. *Nat. Commun.* **9**, 2462 (2018).
26. Hafezi, M., Demler, E. A., Lukin, M. D. & Taylor, J. M. Robust optical delay lines with topological protection. *Nat. Phys.* **7**, 907–912 (2011).
27. Mittal, S., Ganeshan, S., Fan, J., Vaezi, A. & Hafezi, M. Measurement of topological invariants in a 2D photonic system. *Nat. Photon.* **10**, 180–183 (2016).
28. Liu, T. et al. Second-order topological phases in non-Hermitian systems. *Phys. Rev. Lett.* **122**, 076801 (2019).
29. Jing, H., Özdemir, S. K., Lü, H. & Nori, F. High-order exceptional points in optomechanics. *Sci. Rep.* **7**, 3386 (2017).
30. Mittal, S., Goldschmidt, E. A. & Hafezi, M. A topological source of quantum light. *Nature* **561**, 502–506 (2018).
31. Peano, V., Houde, M., Marquardt, F. & Clerk, A. A. Topological quantum fluctuations and traveling wave amplifiers. *Phys. Rev. X* **6**, 041026 (2016).
32. Barik, S. et al. A topological quantum optics interface. *Science* **359**, 666–668 (2018).

Acknowledgements
This research was supported by AFOSR-MURI FA9550-14-1-0267, the Sloan Foundation and the Physics Frontier Center at the Joint Quantum Institute. A.P. and M.A.G. have been supported by the Russian Foundation for Basic Research grant no. 18-29-20037 and the Foundation for the Advancement of Theoretical Physics and Mathematics BASIS. A.P. also acknowledges partial support by the Australian Research Council. The authors thank H. Dehghani, Y. Kivshar and D. Leykam for discussions and E. Yamaguchi and J. Vannucci for experimental help.

Author contributions
S.M. designed the chips and the experiment. S.M. and V.V.O. performed the experiments. A.P., G.Z. and M.A.G. performed the theoretical analysis. M.H. supervised the project. All authors contributed to analysing the data and writing the manuscript.

Competing interests
The authors declare no competing interests.

Additional information
Supplementary information is available for this paper at https://doi.org/10.1038/s41566-019-0452-0.

Reprints and permissions information is available at www.nature.com/reprints.

Correspondence and requests for materials should be addressed to S.M.

Publisher's note: Springer Nature remains neutral with regard to jurisdictional claims in published maps and institutional affiliations.

Methods

Our topological devices were realized using the silicon-on-insulator platform. The ring resonator waveguides were made of silicon and buried in a layer of silicon oxide. The waveguide cross-section was designed to be 510 nm in width and 220 nm in height so that it supported only a single transverse-electric mode at telecom wavelengths (around 1,550 nm). The ring resonators were ~70 µm in length with a free-spectral range of ~1,040 GHz. Therefore, the absorption spectrum of our devices repeats after every free-spectral range (Supplementary Section 9). The coupling gap between the ring waveguides was designed to be 150 nm and 250 nm for the stronger and the weaker couplings, respectively. The devices were fabricated in a standard CMOS fabrication facility at IMEC Belgium.

To measure the power absorption spectra of the devices, we used a fibre-coupled, frequency-tunable, continuous-wave laser. The laser output was coupled to the devices using grating couplers, with a coupling efficiency of ~6 dB per coupler. The unabsorbed light was routed to another grating coupler, collected in a fibre and measured using a photodetector. The measured absorption spectra include the actual power absorbed by the device, the losses introduced by the two grating couplers and also the fibre connectors. These additional losses can be easily measured at frequencies far detuned from the ring resonances where power absorption by the resonators is negligible. The absorption spectra reported in the main text have been corrected for these losses. Moreover, in all our measurements, only a single corner was excited at a given time. The spatial intensity distributions in Figs. 2 and 3 of the main text were summed over the excitations at different corners.

To image the spatial intensity profiles in the lattice, we used a microscope objective (×10) to collect the light scattered from the surface roughness of the ring resonator waveguides. The light was subsequently imaged on a high-sensitivity InGaAs camera (320 × 256 pixels) using a variable-zoom lens system. The raw images, corresponding to Figs. 2d and 3b of the main text, are available in Supplementary Fig. 8.

Data availability

The data that support the findings of this study are available from the corresponding author on reasonable request.

nature photonics

SUPPLEMENTARY INFORMATION
https://doi.org/10.1038/s41566-019-0452-0

In the format provided by the authors and unedited.

Photonic quadrupole topological phases

Sunil Mittal[1,2*], Venkata Vikram Orre[1,2], Guanyu Zhu[1,2], Maxim A. Gorlach[3], Alexander Poddubny[3,4,5] and Mohammad Hafezi[1,2,6]

[1]Joint Quantum Institute, NIST/University of Maryland, College Park, MD, USA. [2]Department of Electrical and Computer Engineering and IREAP, University of Maryland, College Park, MD, USA. [3]ITMO University, St Petersburg, Russia. [4]Nonlinear Physics Centre, Australian National University, Canberra, Australian Capital Territory, Australia. [5]Ioffe Institute, St Petersburg, Russia. [6]Department of Physics, University of Maryland, College Park, MD, USA.
*e-mail: mittals@umd.edu

Supplementary Information: Photonic quadrupole topological phases

Sunil Mittal[1,2], Venkata Vikram Orre[1,2], Guanyu Zhu[1,2],
Maxim A. Gorlach[3], Alexander Poddubny[4,3,5], Mohammad Hafezi[1,2,6]
[1]Joint Quantum Institute, NIST/University of Maryland, College Park, MD 20742, USA
[2]Department of Electrical and Computer Engineering and IREAP,
University of Maryland, College Park, MD 20742, USA
[3]ITMO University, Saint Petersburg 197101, Russia
[4]Nonlinear Physics Centre, Australian National University, Canberra ACT 2601, Australia
[5]Ioffe Institute, Saint Petersburg 194021, Russia
[6]Department of Physics, University of Maryland, College Park, MD 20742, USA

1 Verification of π gauge flux through a unit-cell

To verify that the synthetic gauge flux threading the plaquette is indeed π, we fabricate a single unit-cell of the quadrupole lattice. When the flux $\phi = \pi$, this unit cell exhibits two pairs of degenerate eigenvalues at $\pm\sqrt{2}\gamma$, where γ is the coupling strength between the site rings.[1,2] These eigenvalues can be probed using absorption spectroscopy (Fig.S1a). The measured results for absorption at corners S_1 and S_3 are shown in Fig.S1b. The presence of only two absorption peaks in the spectra confirms the double degeneracy of plaquette eigenmodes which arises due to the gauge flux $\phi = \pi$. The observed asymmetry in the two absorption peaks is because of the disorder-induced frequency mismatch between the ring resonance frequencies. Furthermore, using direct imaging of the spatial intensity profiles (Fig.S1c-f), we observe that an excitation at corner S_1 results in negligible intensity (probability density) at the diagonally opposite corner S_3 and vice-versa. Such intensity distribution is in the agreement with the expected eigenmode structure for a single plaquette and provides another indirect proof that the gauge flux is equal to π. For this single unit-cell device, the coupling strength between the site rings was estimated to be ≈ 26 GHz.

2 Edge Excitation for Quadrupole Device

In addition to the corner modes, the quadrupole topological system also exhibits localized edge states near $\delta\nu = \pm\kappa$.[1,2] The edge states can be probed using waveguide couplers at the edges of the lattice (Fig.S2). Figure S2 shows simulated

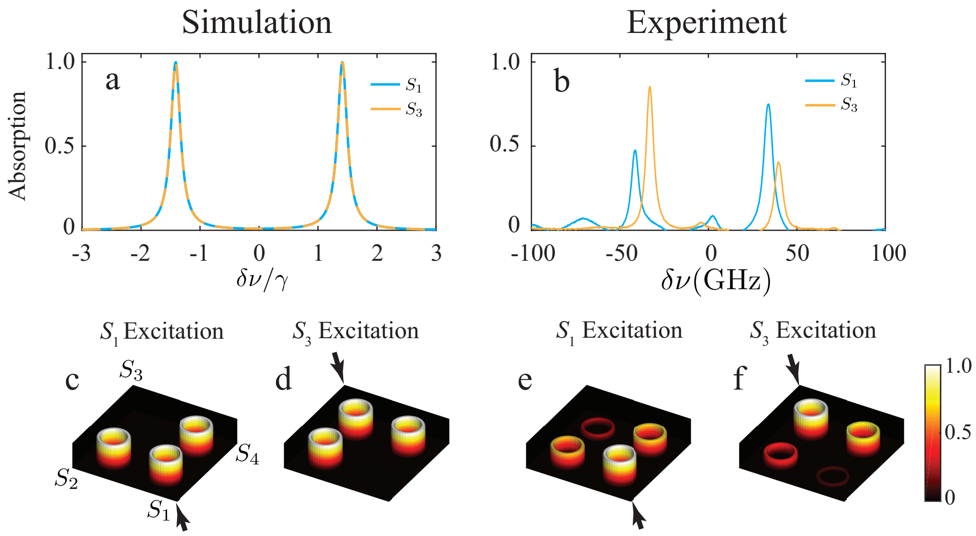

Figure S1: **A unit-cell of the quadrupole lattice. a,b**, Simulated and measured absorption spectrum of the unit-cell, at the two diagonally opposite corners S_1 and S_3. Each spectrum shows only two absorption peaks, consistent with doubly-degenerate energy eigenvalues of a unit-cell of the quadrupole system.[1–3] **c-f**, The corresponding spatial intensity profiles show absence of intensity at corner S_3 when S_1 is excited and vice-versa. The intensity profiles for each excitation is integrated over both absorption peaks.

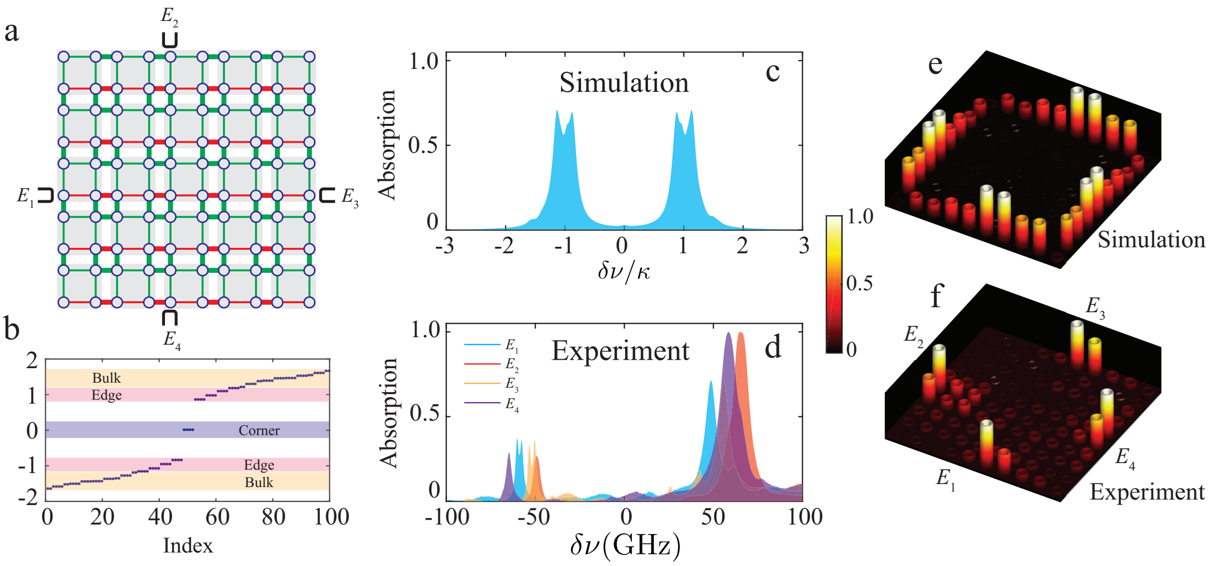

Figure S2: **Edge states in the quadrupole topological lattice. a**, Schematic of the quadrupole device $\left(\frac{\gamma}{\kappa} < 1, \phi = 0\right)$, showing coupler positions for the edge excitations. **b**, Simulated eigenvalue spectra. The edge and the bulk bands are highlighted. **c,d**, Simulated and measured power absorption spectra at the four edges of the device, respectively. The simulated spectra, for a device with no disorder, are four-fold degenerate. **e-f**, Corresponding spatial intensity profiles.

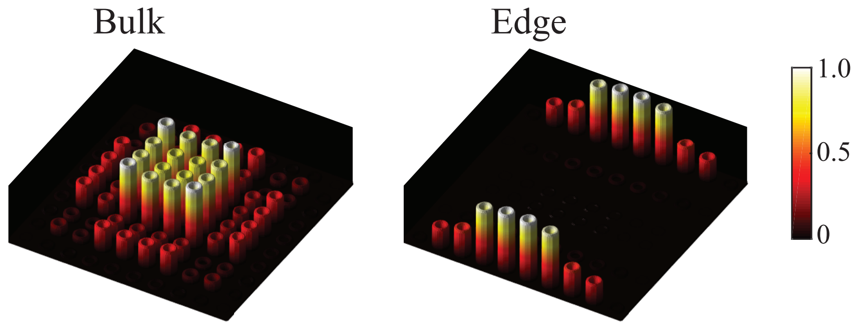

Figure S3: **Overlap of edge and bulk wavefunctions.** **a**, Simulated bulk and **b**, edge wavefunctions in a pure topological device. These wavefunctions do not overlap.

and measured power absorption spectra at the edges and the corresponding spatial intensity profiles in the lattice. In contrast to simulation, we observe two broad absorption peaks near the expected bulk band positions $\left(\delta\nu = \pm\sqrt{2}\kappa\right)$, indicating a coupling between the edge and the bulk states. Also, the observed spatial intensity profile does not match the simulation results (Fig.S2e,f). This is because there is no bandgap between the edge and the bulk bands (Fig.S2b) and therefore, the edge states in this system are not robust against disorder. We note that in a pure topological device with no disorder, the wavefunction of the bulk states does not overlap with those of the edge/corner states (Fig.S3), and therefore, one cannot excite bulk states using excitation at the edge.

3 Characterization of the disorder

The nano-fabrication process introduces various disorders into our devices. The most significant disorder affecting our device is the on-site potential, that is, the mismatch between the site ring resonance frequencies. In addition, there is a disorder in the coupling strengths and also in the gauge flux ϕ, which is essentially a manifestation of the mismatch between link ring resonance frequencies. We used add-drop filters (ADFs) to characterize these disorders and also the coupling strengths γ and κ. The dimensions (length, bend radius) of the ring resonators used in ADFs matched exactly the dimensions of those used in our 2D devices. But, to allow for independent measurements of the coupling strengths, the ADFs had different coupling gaps between the rings and the input-output waveguides. The through and the drop port spectra were measured for five different ADFs (with different coupling strengths) fabricated on each chip. The standard deviation of the resonance frequencies was calculated for each chip and then averaged over ten chips (total fifty ADFs), to give $\sigma_{\nu_0} \approx 32.8$ GHz. The measured contrast and the bandwidth of the spectra yielded

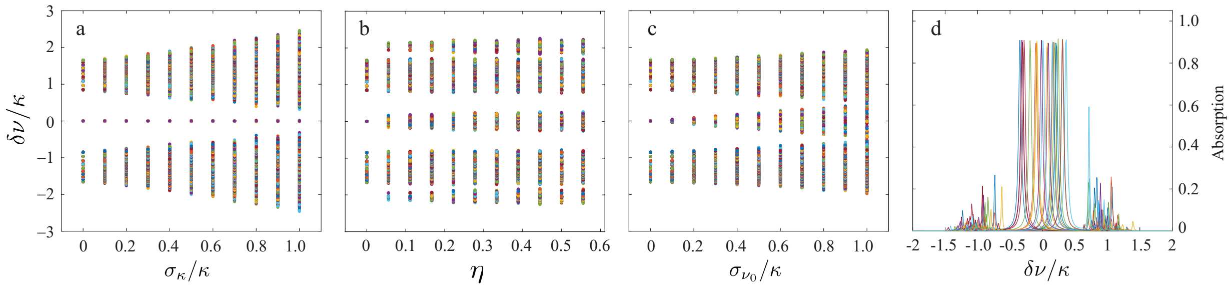

Figure S4: **Robustness of corner states.** Simulated energy-spectra of a 5×5 array of unit cells, as a function of various disorder strengths. **a**, Disorder in coupling strengths (κ, γ), **b**, flipping the sign of of a fraction η of the total (90) couplings along the x-axis (positive to negative or vice-versa), **c**, disorder in ring resonance frequencies (σ_{ν_0}). For each case, we simulate 20 random realizations of disorder. **d**, Simulated absorption spectra for 20 random realizations of disorder, in a 10×10 array of unit cells. We have included the estimated disorder in the coupling strengths, phase and also the ring resonance frequencies.

$\gamma = 4.8$ GHz and $\kappa = 29.0$ GHz as the mean values. The standard deviation in the coupling strengths was $\approx 4\%$. The standard deviation in the gauge flux ϕ was calculated to be ≈ 0.1 using the estimated value of σ_{ν_0}. Also, the loss in the resonators was estimated to be ≈ 1.8 GHz, with a standard deviation of $\approx 20\%$.

4 Robustness of corner states against disorder

To analyze the robustness of the corner states, we numerically calculate the eigen-energies of a 5×5 array of unit cells with varying strengths of disorder in individual parameters. The results are shown in Fig.S4a-c, for 20 random realizations of disorder. We see that the corner state energies are in fact very robust against disorder in coupling strengths (κ and γ). Only when the disorder strength is very strong, comparable to κ, the bandgap closes and the corner states start coupling to edge/bulk states. Similarly, the corner states are also robust against interchange of some of the negative couplings to positive ones (along the x-axis) and vice-versa (Fig.S4b), that is, the bandgap does not close. However, as we increase the fraction (η) of couplings which have been randomly interchanged (of the total 90 couplings between site rings, along the x-axis), we observe that the corner states are no longer degenerate. Finally, we studied their robustness against disorder in the ring resonance frequencies. We see that this on-site potential disorder breaks their degeneracy as well. However, as long as the disorder strength is weak compared to the coupling strength κ, we still observe corner states. We do not expect the parameter fluctuations to increase with the device size. Therefore, using our silicon photonics platform, corner states could easily be realized in much larger arrays (Fig.S4d).

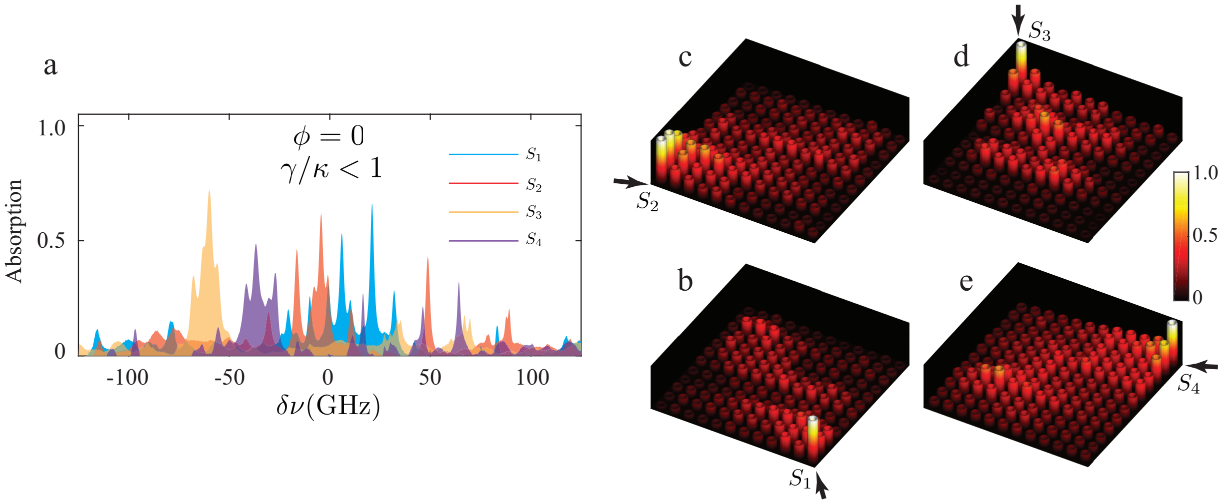

Figure S5: **2D lattice with zero gauge flux. a**, Measured power absorption spectra at the four corners of the device with all positive couplings, that is, $\phi = 0$. **b-e**, Corresponding spatial intensity profiles showing coupling of corner and bulk modes. The intensity profiles are integrated over the absorption peaks.

5 2D Lattice with zero gauge flux

To highlight the robustness of the topological corner states in a quadrupole system, we compare them against those emerging in a system with no gauge flux ($\phi = 0$) which results in zero quadrupole moment (a 2D extension of the Su-Schrieffer-Heeger model, see Section 6). Numerical simulation for such a system ($\phi = 0$) shows sharply localized corner states in the absence of disorder (Fig.4c,e of the main text). However, the measured absorption spectra (Fig.S5) show multi-mode behavior and are consistent with the measured intensity profiles which reveal significant coupling of corner modes to the bulk modes. This clearly demonstrates that the corner states in a system with zero quadrupole moment are not robust against disorder, unlike those associated with quadrupole topological phases.

6 Topological transition realized by varying the gauge flux in the lattice

The proposed integrated silicon photonic platform allows one to realize even richer variety of topological systems by tuning the phase of hopping amplitudes. As an interesting illustration, we examine here the transition between the two-dimensional tight-binding system with all positive couplings with ungapped spectrum and the standard quadrupole insulator characterized by the gapped bands as the magnitude of flux through each plaquette of the lattice is varied from 0 to π.

The schematics of the system under study is shown in Fig. S6a. We assume that the couplings γ and κ are purely

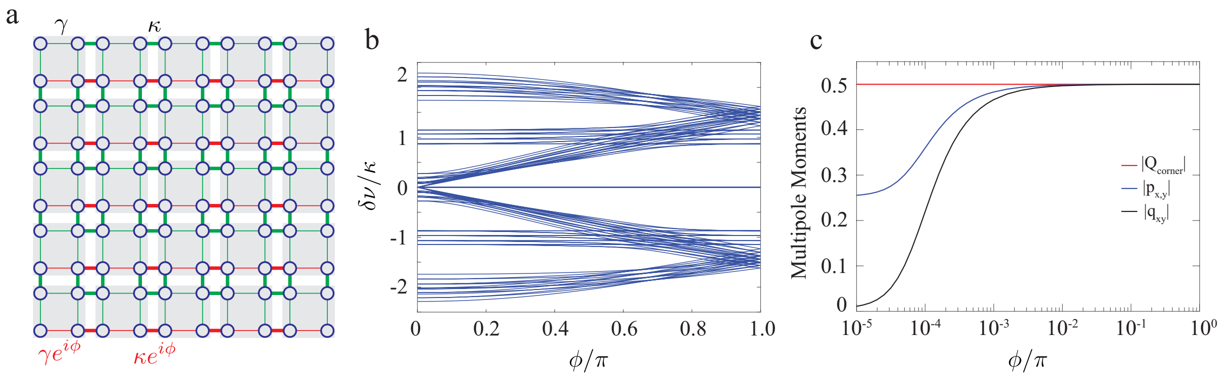

Figure S6: **Variation of gauge flux.** **a**, The schematic of tight-binding system under study realized as an array of evanescently coupled ring resonators. Coupling is ensured via the auxiliary rings. **b**, Numerically computed evolution of the system spectrum as the gauge flux is varied from 0 to π. Opening of a topological gap is observed and the corner states develop. The size of the system is 5×5 unit cells, $\gamma/\kappa = 0.17$. **c**, Corner charge, edge dipole polarizations and bulk quadrupole polarization depending on the flux π. The calculation has been performed for $N = 30$ unit cells, and $\gamma/\kappa = 0.17$. In order to fix the sign of the quadrupole moment the diagonal energies at the diagonal sites of each unit cells were set to $\pm\delta = \pm 10^{-4}\kappa$ Ref.[2]

real, while some of the couplings in the lattice are complex and have an extra hopping phase: $\gamma\, e^{i\phi}$ and $\kappa\, e^{i\phi}$. Note that this geometry ensures ϕ flux through each square plaquette of the lattice. The momentum space Hamiltonian of the periodic structure reads

$$H(k_x, k_y) = \begin{pmatrix} 0 & \gamma + \kappa \mathrm{e}^{ik_y} & 0 & \gamma + \kappa \mathrm{e}^{ik_x} \\ \gamma + \kappa \mathrm{e}^{-ik_y} & 0 & e^{i\phi}(\gamma + \kappa \mathrm{e}^{ik_x}) & 0 \\ 0 & e^{-i\phi}(\gamma + \kappa \mathrm{e}^{-ik_x}) & 0 & \gamma + \kappa \mathrm{e}^{-ik_y} \\ \gamma + \kappa \mathrm{e}^{-ik_x} & 0 & \gamma + \kappa \mathrm{e}^{ik_y} & 0 \end{pmatrix}, \tag{S1}$$

where k_x and k_y are the Cartesian projections of the Bloch wave vector. Similarly to the article main text, we choose the ratio of the hopping amplitudes $\gamma/\kappa = 0.17$.

Zero flux case corresponds to the tight-binding system with all positive couplings which can be viewed as a 2D analogue of the Su-Schrieffer-Heeger (SSH) model.[4–6] The spectrum of this system has no bandgap at zero energy and for that reason does not feature any robust corner states. However, when some of the couplings are made complex such that nonzero gauge flux appears, the bandgap opens and the degenerate corner states emerge, as shown in Fig. S6b. The width of the bandgap grows as the gauge flux is further increased up to π, thus enhancing the robustness of the corner states. The system also hosts one-dimensional edge states at $\delta\nu \approx \pm\kappa$, that are localized at the sides of the square and weakly depend on the flux.

Even more instructive picture is provided by the evolution of dipole and quadrupole polarizations in the system. The dependence of the polarizations on the flux is shown in Fig. S6c. The corner charge $Q_{\rm corner}$ has been calculated for a large 2D system with open boundary conditions at all 4 sides. It was found to be equal to $1/2$ independent of the flux. The dipole polarizations $p_x = p_y$ were evaluated following the procedure in Ref.[2] This calculation involves opening the boundaries along x, using periodic boundary along y direction, and evaluating the dipole polarizations from the averaged positions of the Wannier centers. Next, the bulk quadrupole moment has been evaluated from the equation .

$$Q_{\rm corner} = p_x + p_y - q_{xy} \, . \tag{S2}$$

In agreement with the general theory, Fig. S6c demonstrates, that for the quadrupolar insulator, where $\phi = \pi$, the corner charge is contributed by both quantized dipole polarizations and bulk quadrupole moment. When the flux is unequal to π or 0, the value of q_{xy} in general is not quantized.[2] When the flux decreases the bulk quadrupole moment vanishes and becomes zero in the 2D SSH case, the edge polarizations decrease as well, but the corner charge stays the same. Our calculation indicates that the scale on which the quadrupole moment changes from 0 to $1/2$ is determined by the small on-site potential $\pm\delta = \pm 10^{-4}\kappa$. The energies δ, $-\delta$, δ, $-\delta$ in the clockwise order are added to the sites of the unit cell in order to fix the sign of the corner charges and the quadrupole moment .[2]

The case of zero flux is degenerate and requires special care, since the 2D SSH system is not an insulator, i.e. it lacks a band gap. Our findings of $p_x = p_y = 1/4$, $Q_{\rm corner} = 1/2$ and $q_{xy} = 0$ can be also understood from the results for the anisotropic 2D SSH model with $\kappa_x \neq \kappa_y$ that has a band gap and well-defined polarizations quantized by chiral and inversion symmetries. Namely, in the anisotropic 2D SSH case with $\kappa_x > \kappa_y$ one has $p_x = 1/2$ and $p_y = 0$, while for $\kappa_y > \kappa_x$ the polarizations are $p_y = 1/2$ and $p_x = 0$.[2] The isotropic model with flux tending to zero is an intermediate case where the edge polarizations have to be equal. Thus, averaging the results for $\kappa_x > \kappa_y$ and $\kappa_x < \kappa_y$ we obtain $p_x = p_y = 1/4 = Q_{\rm corner}/2, \quad q_{xy} = 0$, in agreement with the rigorous calculation in Fig. S6c.

The essence of the topological transition as a function of the gauge flux ϕ can be understood with the following symmetry arguments. The quadrupole topological phase is protected by the reflection symmetries along the x and y axes, denoted by M_x and M_y respectively. In order to have protected topological phase and quantized quadrupole moments, one needs to satisfy the following necessary conditions (see Ref.[2] for derivation):

1. $[M_x, H] = [M_y, H] = 0$, i.e., the system Hamiltonian H commutes with the two reflection symmetries.

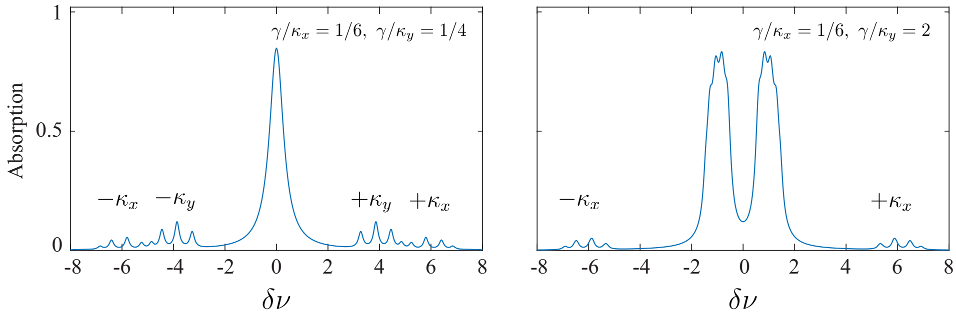

Figure S7: **Quadrupole lattice with asymmetric couplings.** **a**, Simulated absorption spectrum for corner states in a topological system with different hopping strengths along the two axes ($\gamma/\kappa_x = 1/6, \gamma/\kappa_y = 1/4$), and **b**, for a trivial system with ($\gamma/\kappa_x = 1/6, \gamma/\kappa_y = 2$).

2. $[M_x, M_y] \neq 0$, i.e., the two reflection symmetries do not commute. This condition ensures that the edge states are gapped, which is equivalent to gapped "Wannier bands" (see Ref.[2] for the definition and discussion).

It is straightforward to see that the first condition is only satisfied at $\phi = 0, \pi$. Therefore, for any ϕ in between, the quadrupole moment q_{xy} is not quantized and hence not topologically protected, as indicated in Fig. S6c. On the other hand, at the $\phi = 0$ point, the second condition no longer holds, while it is satisfied at the $\phi = \pi$ point due to the introduction of gauge flux. Therefore, the $\phi = 0$ point generically has gapless edge states, or equivalently gapless Wannier bands (in the anisotropic case $\kappa_x \neq \kappa_y$), leading to unprotected corner states. The isotropic case $\kappa_x = \kappa_y$ is special since the bulk band is gapless as stated above, so the Wannier band is not well defined. In this case, the fact that the corner states are unprotected can be attributed to the absence of the bulk band gap.

7 Corner States with asymmetric coupling strengths

In this section, we show numerical simulation for the absorption spectra of a quadrupole device with different hopping strengths $(\gamma_x, \kappa_x, \gamma_y, \kappa_y)$ along the x and the y axis.[2] This system preserves the two mirror symmetries M_x and M_y, but not the C_4 rotation symmetry. Nevertheless, it does exhibit localized corner modes (Fig.S7a). For this simulation, we used $\gamma_x/\kappa_x = 1/6, \gamma_y/\kappa_y = 1/4$ and $\gamma_x = \gamma_y = 1$. We note that for asymmetrical couplings, we see two edge bands on each side of the zero energy peak, at $\pm\kappa_x$ and $\pm\kappa_y$ respectively. Moreover, when one of the couplings is in the trivial regime ($\gamma_x/\kappa_x = 1/6, \gamma_y/\kappa_y = 2$), as expected, we do not observe corner states (Fig.S7b).

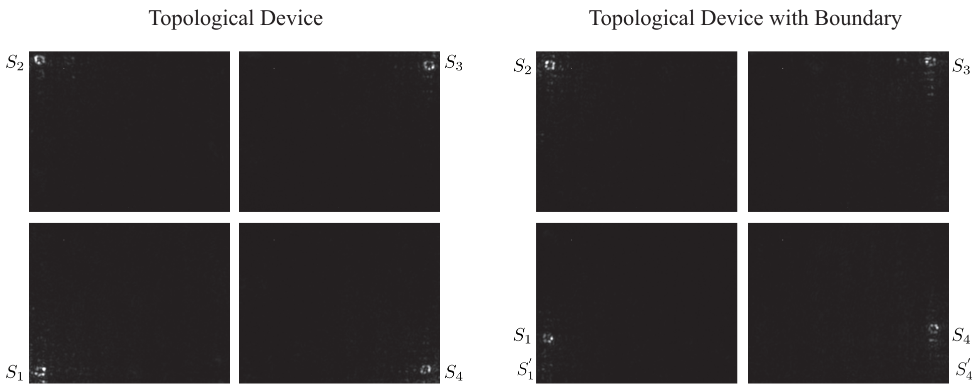

Figure S8: **Raw IR images.** Raw camera images showing corner states for the topological devices reported in Fig.2**d** and Fig.3**d** of the main text.

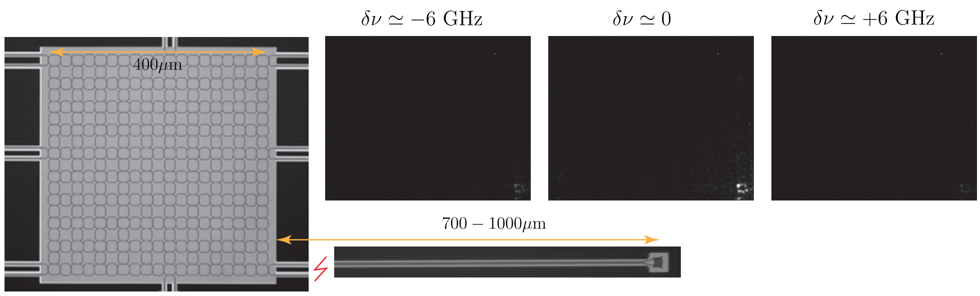

Figure S9: **Microscope image of the lattice and the grating couplers.** Microscope image of the lattice. The coupling waveguides at the corners and the edges can also be seen. The grating couplers are located far from the lattice. Insets: Raw IR images showing intensity in the corner ring as we tune the input light frequency across the resonance.

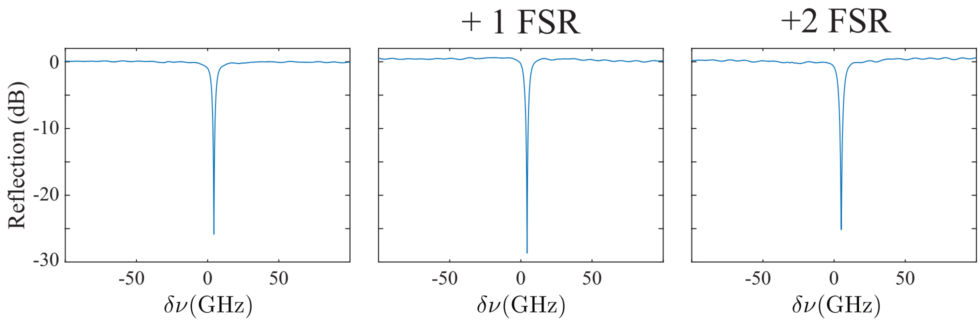

Figure S10: **Free spectral range.** Reflection spectra of the device in three consecutive FSRs.

8 Raw IR images

The raw images IR images collected from the camera, corresponding to Fig.2d and Fig.3b of the main text, are shown in Fig.S8. To suppress scattering from the input, the fiber coupler gratings were positioned very far ($\approx$1 millimeter) from the lattice (Fig.S9) and the camera positions were optimized while imaging different corners. Therefore, when the input light frequency is detuned from the absorption peak of the corner states (even about 10 GHz, the linewidth of the absorption peaks), we do not observe any light intensity in the corner rings (Fig.S9); this confirms that the observed light intensity in the corner rings at resonance is not because of some scattering from the grating couplers.

9 Reflection Spectra

Our devices are designed to operate in the telecom domain, around 1550 nm. The ring resonators are $\approx 70\mu$m in length with a free-spectral range (FSR) of $\approx$ 1040 GHz ($\approx$ 8.3 nm). Therefore, when we sweep the laser frequency, we see that the reflection spectra of the devices repeats itself after every 1040 GHz, the FSR of the site rings. Fig.S10 shows one example of such a reflection measurement ($1-$ Absorption, in dB scale), with a frequency range covering 3 FSRs.

References

1. Benalcazar, W. A., Bernevig, B. A. & Hughes, T. L. Quantized electric multipole insulators. *Science* **357**, 61–66 (2017).

2. Benalcazar, W. A., Bernevig, B. A. & Hughes, T. L. Electric multipole moments, topological multipole moment pumping, and chiral hinge states in crystalline insulators. *Phys. Rev. B* **96**, 245115 (2017).

3. Peterson, C. W., Benalcazar, W. A., Hughes, T. L. & Bahl, G. A quantized microwave quadrupole insulator with topologically protected corner states. *Nature* **555**, 346–350 (2018).

4. Gorlach, M. A. & Poddubny, A. N. Topological edge states of bound photon pairs. *Phys. Rev. A* **95**, 053866 (2017).

5. Di Liberto, M., Recati, A., Carusotto, I. & Menotti, C. Two-body physics in the Su-Schrieffer-Heeger model. *Phys. Rev. A* **94**, 062704 (2016).

6. Gorlach, M. A. *et al.* Simulation of two-boson bound states using arrays of driven-dissipative coupled linear optical resonators. *Phys. Rev. A* **98**, 063625 (2018).

nature photonics

SUPPLEMENTARY INFORMATION

https://doi.org/10.1038/s41566-019-0452-0

In the format provided by the authors and unedited.

Photonic quadrupole topological phases

Sunil Mittal[1,2*], Venkata Vikram Orre[1,2], Guanyu Zhu[1,2], Maxim A. Gorlach[3], Alexander Poddubny[3,4,5] and Mohammad Hafezi[1,2,6]

[1]Joint Quantum Institute, NIST/University of Maryland, College Park, MD, USA. [2]Department of Electrical and Computer Engineering and IREAP, University of Maryland, College Park, MD, USA. [3]ITMO University, St Petersburg, Russia. [4]Nonlinear Physics Centre, Australian National University, Canberra, Australian Capital Territory, Australia. [5]Ioffe Institute, St Petersburg, Russia. [6]Department of Physics, University of Maryland, College Park, MD, USA. *e-mail: mittals@umd.edu

Supplementary Information: Photonic quadrupole topological phases

Sunil Mittal[1,2], Venkata Vikram Orre[1,2], Guanyu Zhu[1,2],
Maxim A. Gorlach[3], Alexander Poddubny[4,3,5], Mohammad Hafezi[1,2,6]
[1]Joint Quantum Institute, NIST/University of Maryland, College Park, MD 20742, USA
[2]Department of Electrical and Computer Engineering and IREAP,
University of Maryland, College Park, MD 20742, USA
[3]ITMO University, Saint Petersburg 197101, Russia
[4]Nonlinear Physics Centre, Australian National University, Canberra ACT 2601, Australia
[5]Ioffe Institute, Saint Petersburg 194021, Russia
[6]Department of Physics, University of Maryland, College Park, MD 20742, USA

1 Verification of π gauge flux through a unit-cell

To verify that the synthetic gauge flux threading the plaquette is indeed π, we fabricate a single unit-cell of the quadrupole lattice. When the flux $\phi = \pi$, this unit cell exhibits two pairs of degenerate eigenvalues at $\pm\sqrt{2}\gamma$, where γ is the coupling strength between the site rings.[1,2] These eigenvalues can be probed using absorption spectroscopy (Fig.S1a). The measured results for absorption at corners S_1 and S_3 are shown in Fig.S1b. The presence of only two absorption peaks in the spectra confirms the double degeneracy of plaquette eigenmodes which arises due to the gauge flux $\phi = \pi$. The observed asymmetry in the two absorption peaks is because of the disorder-induced frequency mismatch between the ring resonance frequencies. Furthermore, using direct imaging of the spatial intensity profiles (Fig.S1c-f), we observe that an excitation at corner S_1 results in negligible intensity (probability density) at the diagonally opposite corner S_3 and vice-versa. Such intensity distribution is in the agreement with the expected eigenmode structure for a single plaquette and provides another indirect proof that the gauge flux is equal to π. For this single unit-cell device, the coupling strength between the site rings was estimated to be ≈ 26 GHz.

2 Edge Excitation for Quadrupole Device

In addition to the corner modes, the quadrupole topological system also exhibits localized edge states near $\delta\nu = \pm\kappa$.[1,2] The edge states can be probed using waveguide couplers at the edges of the lattice (Fig.S2). Figure S2 shows simulated

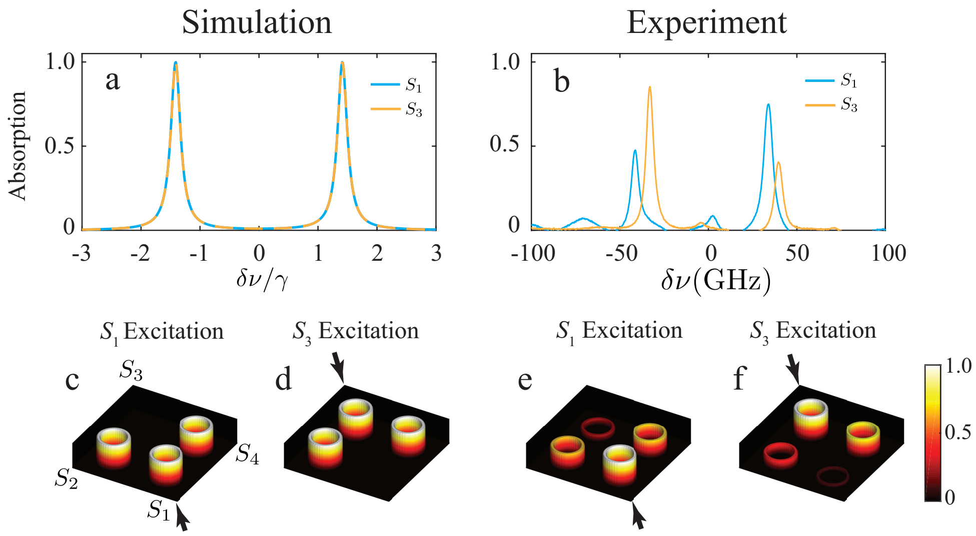

Figure S1: **A unit-cell of the quadrupole lattice. a,b**, Simulated and measured absorption spectrum of the unit-cell, at the two diagonally opposite corners S_1 and S_3. Each spectrum shows only two absorption peaks, consistent with doubly-degenerate energy eigenvalues of a unit-cell of the quadrupole system.[1–3] **c-f**, The corresponding spatial intensity profiles show absence of intensity at corner S_3 when S_1 is excited and vice-versa. The intensity profiles for each excitation is integrated over both absorption peaks.

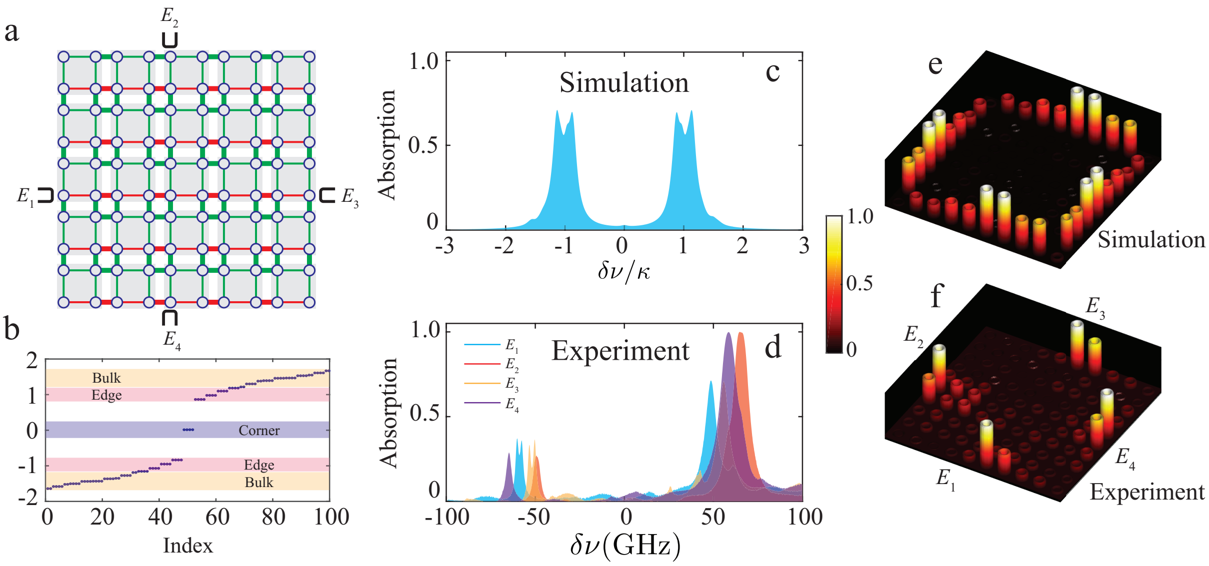

Figure S2: **Edge states in the quadrupole topological lattice. a**, Schematic of the quadrupole device $\left(\frac{\gamma}{\kappa} < 1, \phi = 0\right)$, showing coupler positions for the edge excitations. **b**, Simulated eigenvalue spectra. The edge and the bulk bands are highlighted. **c,d**, Simulated and measured power absorption spectra at the four edges of the device, respectively. The simulated spectra, for a device with no disorder, are four-fold degenerate. **e-f**, Corresponding spatial intensity profiles.

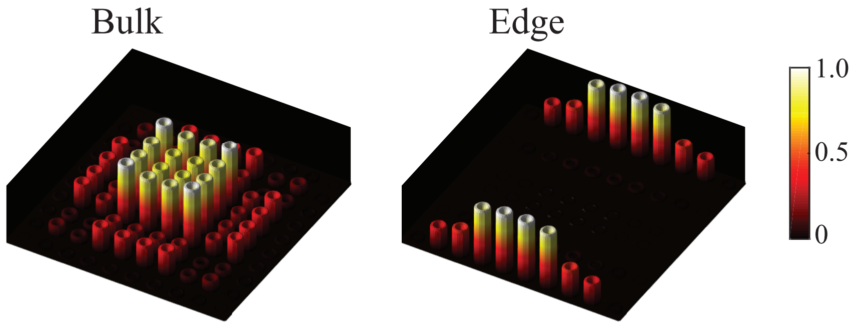

Figure S3: **Overlap of edge and bulk wavefunctions.** **a**, Simulated bulk and **b**, edge wavefunctions in a pure topological device. These wavefunctions do not overlap.

and measured power absorption spectra at the edges and the corresponding spatial intensity profiles in the lattice. In contrast to simulation, we observe two broad absorption peaks near the expected bulk band positions $\left(\delta\nu = \pm\sqrt{2}\kappa\right)$, indicating a coupling between the edge and the bulk states. Also, the observed spatial intensity profile does not match the simulation results (Fig.S2e,f). This is because there is no bandgap between the edge and the bulk bands (Fig.S2b) and therefore, the edge states in this system are not robust against disorder. We note that in a pure topological device with no disorder, the wavefunction of the bulk states does not overlap with those of the edge/corner states (Fig.S3), and therefore, one cannot excite bulk states using excitation at the edge.

3 Characterization of the disorder

The nano-fabrication process introduces various disorders into our devices. The most significant disorder affecting our device is the on-site potential, that is, the mismatch between the site ring resonance frequencies. In addition, there is a disorder in the coupling strengths and also in the gauge flux ϕ, which is essentially a manifestation of the mismatch between link ring resonance frequencies. We used add-drop filters (ADFs) to characterize these disorders and also the coupling strengths γ and κ. The dimensions (length, bend radius) of the ring resonators used in ADFs matched exactly the dimensions of those used in our 2D devices. But, to allow for independent measurements of the coupling strengths, the ADFs had different coupling gaps between the rings and the input-output waveguides. The through and the drop port spectra were measured for five different ADFs (with different coupling strengths) fabricated on each chip. The standard deviation of the resonance frequencies was calculated for each chip and then averaged over ten chips (total fifty ADFs), to give $\sigma_{\nu_0} \approx 32.8$ GHz. The measured contrast and the bandwidth of the spectra yielded

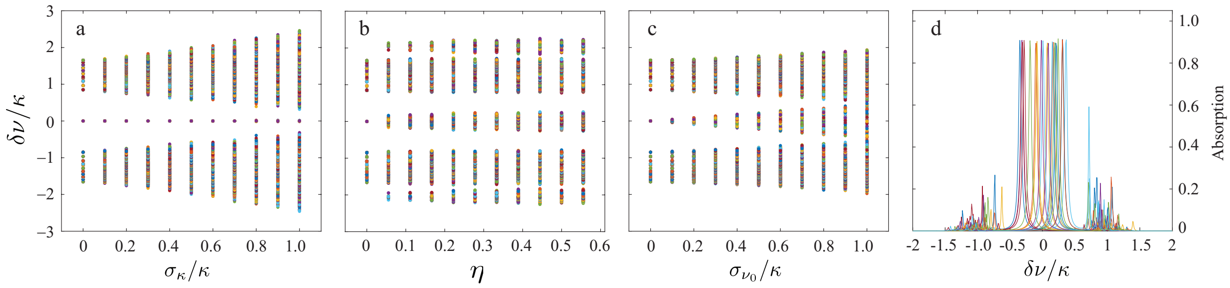

Figure S4: **Robustness of corner states.** Simulated energy-spectra of a 5×5 array of unit cells, as a function of various disorder strengths. **a**, Disorder in coupling strengths (κ, γ), **b**, flipping the sign of of a fraction η of the total (90) couplings along the x-axis (positive to negative or vice-versa), **c**, disorder in ring resonance frequencies (σ_{ν_0}). For each case, we simulate 20 random realizations of disorder. **d**, Simulated absorption spectra for 20 random realizations of disorder, in a 10×10 array of unit cells. We have included the estimated disorder in the coupling strengths, phase and also the ring resonance frequencies.

$\gamma = 4.8$ GHz and $\kappa = 29.0$ GHz as the mean values. The standard deviation in the coupling strengths was $\approx 4\%$. The standard deviation in the gauge flux ϕ was calculated to be ≈ 0.1 using the estimated value of σ_{ν_0}. Also, the loss in the resonators was estimated to be ≈ 1.8 GHz, with a standard deviation of $\approx 20\%$.

4 Robustness of corner states against disorder

To analyze the robustness of the corner states, we numerically calculate the eigen-energies of a 5×5 array of unit cells with varying strengths of disorder in individual parameters. The results are shown in Fig.S4a-c, for 20 random realizations of disorder. We see that the corner state energies are in fact very robust against disorder in coupling strengths (κ and γ). Only when the disorder strength is very strong, comparable to κ, the bandgap closes and the corner states start coupling to edge/bulk states. Similarly, the corner states are also robust against interchange of some of the negative couplings to positive ones (along the x-axis) and vice-versa (Fig.S4b), that is, the bandgap does not close. However, as we increase the fraction (η) of couplings which have been randomly interchanged (of the total 90 couplings between site rings, along the x-axis), we observe that the corner states are no longer degenerate. Finally, we studied their robustness against disorder in the ring resonance frequencies. We see that this on-site potential disorder breaks their degeneracy as well. However, as long as the disorder strength is weak compared to the coupling strength κ, we still observe corner states. We do not expect the parameter fluctuations to increase with the device size. Therefore, using our silicon photonics platform, corner states could easily be realized in much larger arrays (Fig.S4d).

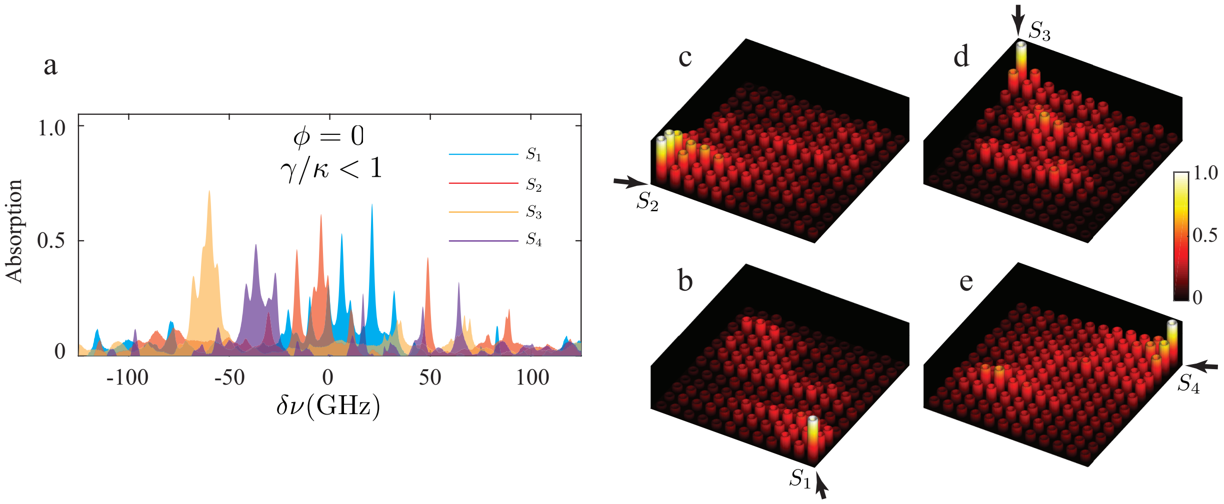

Figure S5: **2D lattice with zero gauge flux. a**, Measured power absorption spectra at the four corners of the device with all positive couplings, that is, $\phi = 0$. **b-e**, Corresponding spatial intensity profiles showing coupling of corner and bulk modes. The intensity profiles are integrated over the absorption peaks.

5 2D Lattice with zero gauge flux

To highlight the robustness of the topological corner states in a quadrupole system, we compare them against those emerging in a system with no gauge flux ($\phi = 0$) which results in zero quadrupole moment (a 2D extension of the Su-Schrieffer-Heeger model, see Section 6). Numerical simulation for such a system ($\phi = 0$) shows sharply localized corner states in the absence of disorder (Fig.4c,e of the main text). However, the measured absorption spectra (Fig.S5) show multi-mode behavior and are consistent with the measured intensity profiles which reveal significant coupling of corner modes to the bulk modes. This clearly demonstrates that the corner states in a system with zero quadrupole moment are not robust against disorder, unlike those associated with quadrupole topological phases.

6 Topological transition realized by varying the gauge flux in the lattice

The proposed integrated silicon photonic platform allows one to realize even richer variety of topological systems by tuning the phase of hopping amplitudes. As an interesting illustration, we examine here the transition between the two-dimensional tight-binding system with all positive couplings with ungapped spectrum and the standard quadrupole insulator characterized by the gapped bands as the magnitude of flux through each plaquette of the lattice is varied from 0 to π.

The schematics of the system under study is shown in Fig. S6a. We assume that the couplings γ and κ are purely

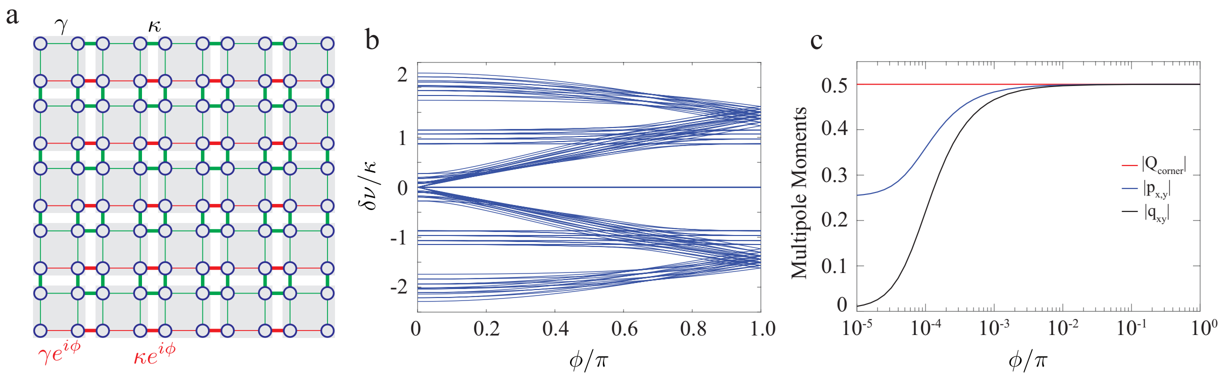

Figure S6: **Variation of gauge flux.** **a**, The schematic of tight-binding system under study realized as an array of evanescently coupled ring resonators. Coupling is ensured via the auxiliary rings. **b**, Numerically computed evolution of the system spectrum as the gauge flux is varied from 0 to π. Opening of a topological gap is observed and the corner states develop. The size of the system is 5×5 unit cells, $\gamma/\kappa = 0.17$. **c**, Corner charge, edge dipole polarizations and bulk quadrupole polarization depending on the flux π. The calculation has been performed for $N = 30$ unit cells, and $\gamma/\kappa = 0.17$. In order to fix the sign of the quadrupole moment the diagonal energies at the diagonal sites of each unit cells were set to $\pm\delta = \pm 10^{-4}\kappa$ Ref.[2]

real, while some of the couplings in the lattice are complex and have an extra hopping phase: $\gamma\, e^{i\phi}$ and $\kappa\, e^{i\phi}$. Note that this geometry ensures ϕ flux through each square plaquette of the lattice. The momentum space Hamiltonian of the periodic structure reads

$$H(k_x, k_y) = \begin{pmatrix} 0 & \gamma + \kappa \mathrm{e}^{ik_y} & 0 & \gamma + \kappa \mathrm{e}^{ik_x} \\ \gamma + \kappa e^{-ik_y} & 0 & e^{i\phi}(\gamma + \kappa \mathrm{e}^{ik_x}) & 0 \\ 0 & e^{-i\phi}(\gamma + \kappa \mathrm{e}^{-ik_x}) & 0 & \gamma + \kappa \mathrm{e}^{-ik_y} \\ \gamma + \kappa e^{-ik_x} & 0 & \gamma + \kappa \mathrm{e}^{ik_y} & 0 \end{pmatrix}, \tag{S1}$$

where k_x and k_y are the Cartesian projections of the Bloch wave vector. Similarly to the article main text, we choose the ratio of the hopping amplitudes $\gamma/\kappa = 0.17$.

Zero flux case corresponds to the tight-binding system with all positive couplings which can be viewed as a 2D analogue of the Su-Schrieffer-Heeger (SSH) model.[4–6] The spectrum of this system has no bandgap at zero energy and for that reason does not feature any robust corner states. However, when some of the couplings are made complex such that nonzero gauge flux appears, the bandgap opens and the degenerate corner states emerge, as shown in Fig. S6b. The width of the bandgap grows as the gauge flux is further increased up to π, thus enhancing the robustness of the corner states. The system also hosts one-dimensional edge states at $\delta\nu \approx \pm\kappa$, that are localized at the sides of the square and weakly depend on the flux.

Even more instructive picture is provided by the evolution of dipole and quadrupole polarizations in the system. The dependence of the polarizations on the flux is shown in Fig. S6c. The corner charge $Q_{\rm corner}$ has been calculated for a large 2D system with open boundary conditions at all 4 sides. It was found to be equal to $1/2$ independent of the flux. The dipole polarizations $p_x = p_y$ were evaluated following the procedure in Ref.[2] This calculation involves opening the boundaries along x, using periodic boundary along y direction, and evaluating the dipole polarizations from the averaged positions of the Wannier centers. Next, the bulk quadrupole moment has been evaluated from the equation .

$$Q_{\rm corner} = p_x + p_y - q_{xy} \ . \tag{S2}$$

In agreement with the general theory, Fig. S6c demonstrates, that for the quadrupolar insulator, where $\phi = \pi$, the corner charge is contributed by both quantized dipole polarizations and bulk quadrupole moment. When the flux is unequal to π or 0, the value of q_{xy} in general is not quantized.[2] When the flux decreases the bulk quadrupole moment vanishes and becomes zero in the 2D SSH case, the edge polarizations decrease as well, but the corner charge stays the same. Our calculation indicates that the scale on which the quadrupole moment changes from 0 to $1/2$ is determined by the small on-site potential $\pm\delta = \pm 10^{-4}\kappa$. The energies δ, $-\delta$, δ, $-\delta$ in the clockwise order are added to the sites of the unit cell in order to fix the sign of the corner charges and the quadrupole moment .[2]

The case of zero flux is degenerate and requires special care, since the 2D SSH system is not an insulator, i.e. it lacks a band gap. Our findings of $p_x = p_y = 1/4$, $Q_{\rm corner} = 1/2$ and $q_{xy} = 0$ can be also understood from the results for the anisotropic 2D SSH model with $\kappa_x \neq \kappa_y$ that has a band gap and well-defined polarizations quantized by chiral and inversion symmetries. Namely, in the anisotropic 2D SSH case with $\kappa_x > \kappa_y$ one has $p_x = 1/2$ and $p_y = 0$, while for $\kappa_y > \kappa_x$ the polarizations are $p_y = 1/2$ and $p_x = 0$.[2] The isotropic model with flux tending to zero is an intermediate case where the edge polarizations have to be equal. Thus, averaging the results for $\kappa_x > \kappa_y$ and $\kappa_x < \kappa_y$ we obtain $p_x = p_y = 1/4 = Q_{\rm corner}/2, \quad q_{xy} = 0$, in agreement with the rigorous calculation in Fig. S6c.

The essence of the topological transition as a function of the gauge flux ϕ can be understood with the following symmetry arguments. The quadrupole topological phase is protected by the reflection symmetries along the x and y axes, denoted by M_x and M_y respectively. In order to have protected topological phase and quantized quadrupole moments, one needs to satisfy the following necessary conditions (see Ref.[2] for derivation):

1. $[M_x, H] = [M_y, H] = 0$, i.e., the system Hamiltonian H commutes with the two reflection symmetries.

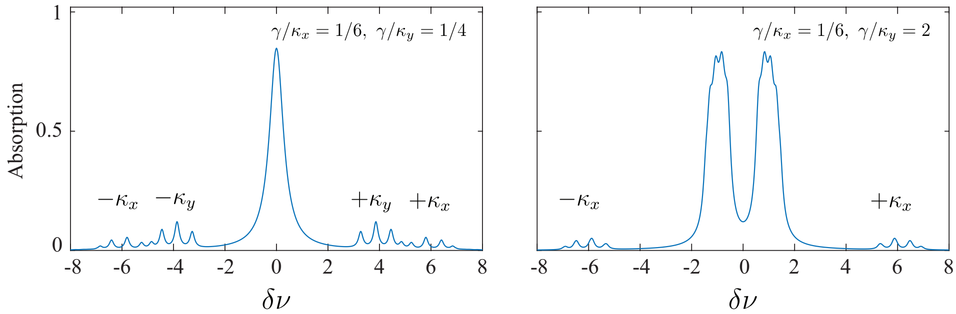

Figure S7: **Quadrupole lattice with asymmetric couplings. a**, Simulated absorption spectrum for corner states in a topological system with different hopping strengths along the two axes ($\gamma/\kappa_x = 1/6, \gamma/\kappa_y = 1/4$), and **b**, for a trivial system with ($\gamma/\kappa_x = 1/6, \gamma/\kappa_y = 2$).

2. $[M_x, M_y] \neq 0$, i.e., the two reflection symmetries do not commute. This condition ensures that the edge states are gapped, which is equivalent to gapped "Wannier bands" (see Ref.[2] for the definition and discussion).

It is straightforward to see that the first condition is only satisfied at $\phi = 0, \pi$. Therefore, for any ϕ in between, the quadrupole moment q_{xy} is not quantized and hence not topologically protected, as indicated in Fig. S6c. On the other hand, at the $\phi = 0$ point, the second condition no longer holds, while it is satisfied at the $\phi = \pi$ point due to the introduction of gauge flux. Therefore, the $\phi = 0$ point generically has gapless edge states, or equivalently gapless Wannier bands (in the anisotropic case $\kappa_x \neq \kappa_y$), leading to unprotected corner states. The isotropic case $\kappa_x = \kappa_y$ is special since the bulk band is gapless as stated above, so the Wannier band is not well defined. In this case, the fact that the corner states are unprotected can be attributed to the absence of the bulk band gap.

7 Corner States with asymmetric coupling strengths

In this section, we show numerical simulation for the absorption spectra of a quadrupole device with different hopping strengths $(\gamma_x, \kappa_x, \gamma_y, \kappa_y)$ along the x and the y axis.[2] This system preserves the two mirror symmetries M_x and M_y, but not the C_4 rotation symmetry. Nevertheless, it does exhibit localized corner modes (Fig.S7a). For this simulation, we used $\gamma_x/\kappa_x = 1/6, \gamma_y/\kappa_y = 1/4$ and $\gamma_x = \gamma_y = 1$. We note that for asymmetrical couplings, we see two edge bands on each side of the zero energy peak, at $\pm\kappa_x$ and $\pm\kappa_y$ respectively. Moreover, when one of the couplings is in the trivial regime ($\gamma_x/\kappa_x = 1/6, \gamma_y/\kappa_y = 2$), as expected, we do not observe corner states (Fig.S7b).

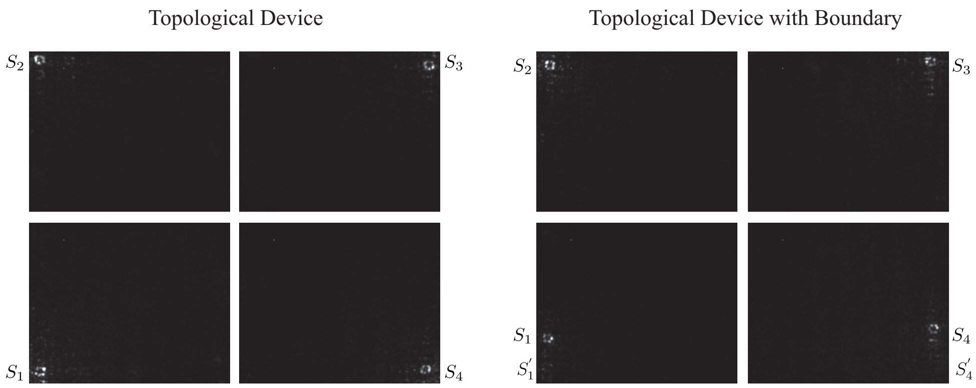

Figure S8: **Raw IR images.** Raw camera images showing corner states for the topological devices reported in Fig.2**d** and Fig.3**d** of the main text.

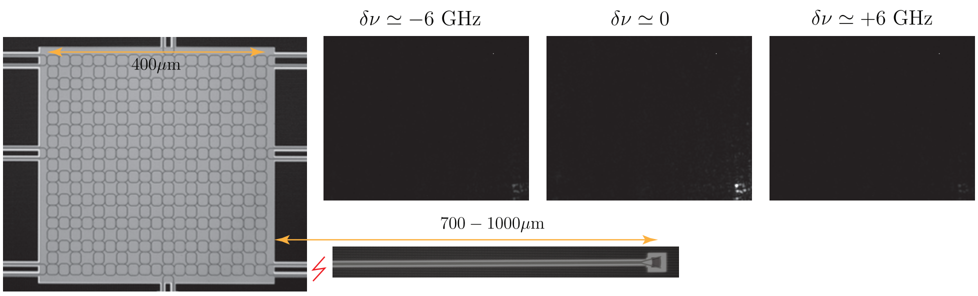

Figure S9: **Microscope image of the lattice and the grating couplers.** Microscope image of the lattice. The coupling waveguides at the corners and the edges can also be seen. The grating couplers are located far from the lattice. Insets: Raw IR images showing intensity in the corner ring as we tune the input light frequency across the resonance.

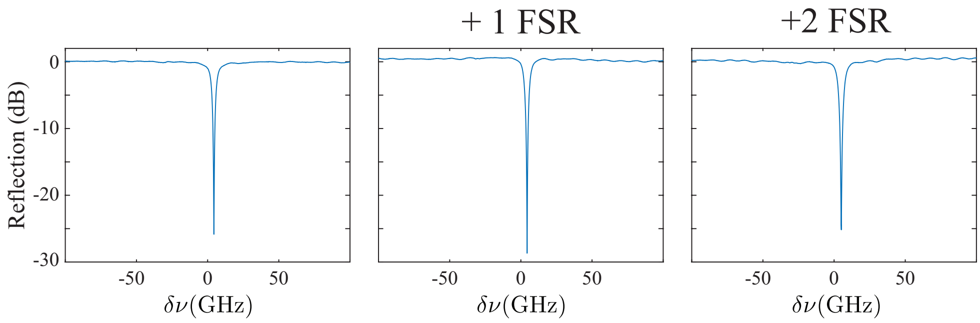

Figure S10: **Free spectral range.** Reflection spectra of the device in three consecutive FSRs.

8 Raw IR images

The raw images IR images collected from the camera, corresponding to Fig.2d and Fig.3b of the main text, are shown in Fig.S8. To suppress scattering from the input, the fiber coupler gratings were positioned very far (≈1 millimeter) from the lattice (Fig.S9) and the camera positions were optimized while imaging different corners. Therefore, when the input light frequency is detuned from the absorption peak of the corner states (even about 10 GHz, the linewidth of the absorption peaks), we do not observe any light intensity in the corner rings (Fig.S9); this confirms that the observed light intensity in the corner rings at resonance is not because of some scattering from the grating couplers.

9 Reflection Spectra

Our devices are designed to operate in the telecom domain, around 1550 nm. The ring resonators are $\approx 70\mu$m in length with a free-spectral range (FSR) of ≈ 1040 GHz $(\approx 8.3$ nm$)$. Therefore, when we sweep the laser frequency, we see that the reflection spectra of the devices repeats itself after every 1040 GHz, the FSR of the site rings. Fig.S10 shows one example of such a reflection measurement ($1 -$ Absorption, in dB scale), with a frequency range covering 3 FSRs.

References

1. Benalcazar, W. A., Bernevig, B. A. & Hughes, T. L. Quantized electric multipole insulators. *Science* **357**, 61–66 (2017).

2. Benalcazar, W. A., Bernevig, B. A. & Hughes, T. L. Electric multipole moments, topological multipole moment pumping, and chiral hinge states in crystalline insulators. *Phys. Rev. B* **96**, 245115 (2017).

3. Peterson, C. W., Benalcazar, W. A., Hughes, T. L. & Bahl, G. A quantized microwave quadrupole insulator with topologically protected corner states. *Nature* **555**, 346–350 (2018).

4. Gorlach, M. A. & Poddubny, A. N. Topological edge states of bound photon pairs. *Phys. Rev. A* **95**, 053866 (2017).

5. Di Liberto, M., Recati, A., Carusotto, I. & Menotti, C. Two-body physics in the Su-Schrieffer-Heeger model. *Phys. Rev. A* **94**, 062704 (2016).

6. Gorlach, M. A. *et al.* Simulation of two-boson bound states using arrays of driven-dissipative coupled linear optical resonators. *Phys. Rev. A* **98**, 063625 (2018).